# Supporting Information

## Kosaka et al. 10.1073/pnas.1215582110

### SI Text

### SI Materials and Methods

**Coupled Seasonal Prediction Models.** We examine 14 coupled general circulation models (GCMs) from around the world, initialized on May 1 each year. Here we use hindcasts by prediction models used in Climate Prediction and its Application to Society (CliPAS) and Development of a European Multimodel Ensemble System for Seasonal to Interannual Prediction (DEMETER) projects. CliPAS models include those from the Bureau of Meteorology Research Centre (BMRC), Australia (1980–2002, 10 members); the Geophysical Fluid Dynamics Laboratory (GFDL), United States (1979–2005, 10 members); the Japan Meteorological Agency (JMA) (1979–2008, 5 members); the National Centers for Environmental Prediction (NCEP), United States (1981–2003, 15 members); Pusan National University (PNU), Korea (1979–2011, 5 members); Seoul National University (SNU), Korea (1980–2001, 6 members); and University of Hawaii (UH), United States (1982–2003, 10 members). DEMETER models are those from the European Centre for Research and Advanced Training in Scientific Computation (CERFACS), France; the European Centre for Medium-Range Weather Forecasts (ECMWF); Istituto Nazionale de Geofisica e Vulcanologia (INGV), Italy; Laboratoire d'Océanographie Dynamique et de Climatologie, (LODYC), France; Météo-France; Max-Planck Institut für Meteorologie (MPI), Germany; and UK Met Office (UKMO). For all DEMETER predictions, we use 9-member ensembles for 1980–2001. We analyze the multimodel ensemble (MME) of CliPAS and DEMETER models for a common period of 1982–2001. All of the prediction data are given on a 2.5° × 2.5° grid.

**Vorticity.** To focus on large-scale features, we have applied a horizontal smoothing to relative vorticity by multiplying a spherical harmonic component of the total wavenumber $n$ by $\exp\{-K[n(n+1)]^2\}$, where the coefficient $K$ has been set in such a way that the harmonic component of $n = 24$ is reduced by 50%.

**Tropospheric Temperature.** We have defined tropospheric temperature as temperature averaged between 850- and 250-hPa levels. To focus on anomaly structure rather than entire tropical warming induced by El Niño–Southern Oscillation (ENSO), we have removed the tropical (30°S–30°N) average of tropospheric temperature before evaluating correlations in Figs. 4*G* and 5*A*.

**Atmosphere-Induced Latent Heat Flux.** Latent heat flux (or evaporation) $E$ changes due to both atmospheric conditions and sea surface temperature (SST). We evaluate the SST-induced latent heat flux anomaly $E'_{SST}$ by linearizing the bulk formula as

$$E'_{SST} = \overline{E}(dq_s/q_s dT)T',$$

where the overbar indicates climatology. $q_s(T)$ denotes saturated specific humidity that follows the Clausius–Clapeyron relationship. We obtain the atmosphere-induced evaporation anomaly as $E' - E'_{SST}$ (1) and plot it in Fig. 4 and Figs. S4–S6.

**Other Notes on Analyses.** We have linearly detrended observational, Pacific Ocean–Global Atmosphere (POGA), and seasonal hindcast data before all of the analyses. We test statistical significance and estimate intervals by a $t$ statistic and errors of empirical orthogonal function (EOF) variance by North's rule (2).

### Observed Anomalies Associated with the Pacific–Japan Pattern

The Pacific–Japan (PJ) pattern features a meridional dipole of surface circulation anomalies over the Northwestern Pacific (NWP) (Fig. S1*A*). The anomalous circulation penetrates into the upper troposphere with a poleward phase tilt (Fig. S1*B*). In the particular polarity shown in Fig. S1, the pattern lowers surface air temperature over broad regions of China, Korea, and Japan (Fig. S1*C*) by anomalous temperature advection and insolation. SST is anomalously warm over the South China Sea (SCS) and the tropical NWP whereas it is cool in the midlatitudes.

The pattern is also associated with seasonal-mean tropical cyclone (TC) occurrence (Fig. S1*D*). Here we define TC occurrence when a grid point is within 500 km from centers of TCs or TC-originated extratropical cyclones in June–July–August (JJA). The change in TC occurrence is largely attributable to the number of TC geneses in summer (Fig. S1*E*). We have also evaluated TC genesis potential (GP) (3). Correlation between the PJ pattern and GP is –0.58 (significant at $P < 0.01$), suggesting that the PJ pattern significantly changes the condition for TC genesis. Despite the fact that warm SST anomalies cover a large part of the tropical NWP (Fig. S1*C*), their contribution to the GP anomaly is very small, and atmospheric anomalies mostly determine GP anomalies.

### Robustness of the PJ Pattern in Model Experiments

We have repeated the EOF analysis to POGA ensemble-mean, intermember, and total (ensemble-mean plus intermember) variability, the ENSO-suppressed coupled GCM experiment (NoENSO) and the atmospheric GCM experiment with climatological SST (aCLIM). POGA is skillful in reproducing the PJ pattern, as EOF1 of POGA total variance shows a high spatial correlation with the observational counterpart (Table S1). Furthermore, the EOF1 patterns derived from other variability components/experiments are mutually similar (Table S1).

The observed summer PJ pattern significantly correlates with ENSO in the preceding boreal winter (Fig. S2*A*). The POGA experiment reproduces the association of the PJ pattern and ENSO (Fig. S2 *C* and *D*). Fig. S2 *E* and *F* confirms that the PJ pattern in NoENSO lacks significant SST anomalies over the equatorial eastern Pacific.

### Atmospheric Responses to Diabatic Heating over the Northern Indian Ocean and Tropical NWP

In the PJ–Indian Ocean (IO) mode, atmospheric Rossby and Kelvin waves mediate SST in the northern IO to the west and the PJ pattern over the NWP to the east. Warm SST over the northern IO heats the troposphere via moist adiabatic adjustment, whereas precipitation decrease over the tropical NWP cools the atmosphere. To examine atmospheric response to these forcings, we have performed experiments with a linear baroclinic model (LBM) (4, 5). The model is linearized about the observed JJA climatology and forced by prescribed diabatic heating centered at the mid-troposphere. We have integrated the model for 60 d and show its quasi-stationary response as averages for the last 30 d.

Diabatic cooling over the tropical NWP forces cold anomalies centered northwest of the cooling, in the form of a cold Rossby wave (Fig. S3*A*) (6, 7). Due to its westward-propagating phase velocity, the low-level easterly response extends westward to the northern IO (Fig. S3*A*), weakening the climatological westerlies. It also forces surface northeasterlies reaching to the Maritime Continent.

Despite equatorial asymmetry, the northern IO heating induces equatorially symmetric warming of tropospheric temperature

extending eastward, characteristic of the Kelvin wave (Fig. S3*B*). The response is accompanied by low-level easterlies over the tropical western Pacific and the IO, with a stronger signal over the northern than the southern IO. The easterly response over the Bay of Bengal and eastern Arabian Sea can reinforce westward expansion of the PJ tropical lobe induced by the NWP cooling and feeds back to the northern IO warming. The surface wind is divergent over the tropical NWP east of the Philippines, helping suppress the local convection. Experiments with atmospheric general circulation models yielded similar results (8, 9).

### Shortwave Radiation Anomalies in the PJIO Mode

Fig. S4*A* shows downward shortwave radiation anomalies at the surface associated with the PJ pattern in NoENSO. In accord with the westward intrusion of the cold Rossby wave, the lower cloudiness region also extends from the tropical NWP to the Bay of Bengal. The resultant increase in shortwave radiation is comparable in magnitude with that of anomalous latent heat flux (Fig. 4*A*), and both contribute to the northern IO warming (Fig. S4*B*).

### PJIO Coupled Mode in Observations

To extract the PJIO-coupled mode in observations, we chose seasonal PJ events in which the seasonal-mean leading principal component (PC1) exceeds ±0.5 times its SD, either positively or negatively, whereas Niño 3.4 SST anomalies in the preceding November–December–January (NDJ) and concurrent JJA are both within ±0.7 times their SDs. This procedure picks up three positive (1980, 1993, and 1996) and five negative (1981, 1986, 1990, 1994, and 2004) PJ events. Fig. S5 shows the composited difference. Without SST anomalies in the equatorial Pacific east of the dateline (Fig. S5 *B* and *C*), the PJ pattern is still associated with the northern IO warming and atmospheric warm Kelvin and cold Rossby waves (Fig. S5*A*). The surface wind anomalies suppress evaporation and warm the northern IO. The overall features are consistent with the PJIO mode in NoENSO (Fig. 4 *A* and *B*). Similar features are obvious with a severer criterion to choose non-ENSO years (10), with two positive (1980 and 1993) and three negative (1981, 1986, and 1990) events (Fig. S6).

### Coupled PJIO Mode in Seasonal Predictions

We examine the PJIO mode in NoENSO and ensemble seasonal hindcasts by 14 coupled GCMs. In singular value decomposition (SVD) analysis applied to intermember variance for each prediction model (Fig. S7 *C*–*P*) and the 14-model grand ensemble of intermember variance (Fig. S7*B* and Fig. 5 *E* and *F*), almost all of the models feature IO warming and a precipitation dipole between the IO and the tropical NWP as their leading SVD modes (SVD1s), similar to the NoENSO results (Fig. S7*A*). SVD1s explain large parts of intermember covariance. In most models the lead–lag correlation between SST and vorticity time series maximizes at zero lag (Fig. S8), confirming the coupled nature of the SVD1s. PJIO-like ocean–atmospheric anomalies dominate intermember spreads of a NWP monsoon index in a smaller set of seasonal prediction models (11).

### Reduction of Intermember PJ Variance by Decoupling

We have conducted another experiment with Atmospheric Model Version 2.1 (AM2.1), where nine-member runs are forced with POGA ensemble-mean SST globally. Its intermember variance projected onto EOF1 of POGA total variance significantly drops by 24% from that of intermember POGA in seasonal mean, confirming that decoupling underestimates ensemble spread of the PJ pattern.


1. Du Y, Xie S-P, Huang G, Hu K (2009) Role of air–sea interaction in the long persistence of El Niño-induced north Indian Ocean warming. *J Clim* 22(8):2023–2038.
2. North GR, Bell TL, Cahalan RF, Moeng FJ (1982) Sampling errors in the estimation of empirical orthogonal functions. *Mon Weather Rev* 110(7):699–706.
3. Emanuel KA, Nolan DS (2004) Tropical cyclone activity and global climate. *26th Conference on Hurricanes and Tropical Meteorology, Miami, FL* (American Meteorological Society, Boston), pp 240–241. Available at https://ams.confex.com/ams/26HURR/techprogram/paper_75463.htm.
4. Watanabe M, Kimoto M (2000) Atmosphere-ocean thermal coupling in the North Atlantic: A positive feedback. *Q J R Meteorol Soc* 126(570):3343–3369.
5. Watanabe M, Kimoto M (2001) Corrigendum. *Q J R Meteorol Soc* 127(572):733–734.
6. Matsuno T (1966) Quasi-geostrophic motions in the equatorial area. *J Meteorol Soc Jpn* 44(1):25–43.
7. Gill AE (1980) Some simple solutions for heat-induced tropical circulation. *Q J R Meteorol Soc* 106(449):447–462.
8. Ohba M, Ueda H (2006) A role of zonal gradient of SST between the Indian Ocean and the western Pacific in localized convection around the Philippines. *SOLA* 2:176–179.
9. Xie S-P, et al. (2009) Indian Ocean capacitor effect on Indo-western Pacific climate during the summer following El Niño. *J Clim* 22(3):730–747.
10. Wu B, Zhou T, Li T (2009) Contrast of rainfall-SST relationships in the western North Pacific between the ENSO-developing and ENSO-decaying summers. *J Clim* 22(16):4398–4405.
11. Li C, Lu R, Dong B (2012) Predictability of the western North Pacific summer climate demonstrated by the coupled models of ENSEMBLES. *Clim Dyn* 39(1-2):329–346.

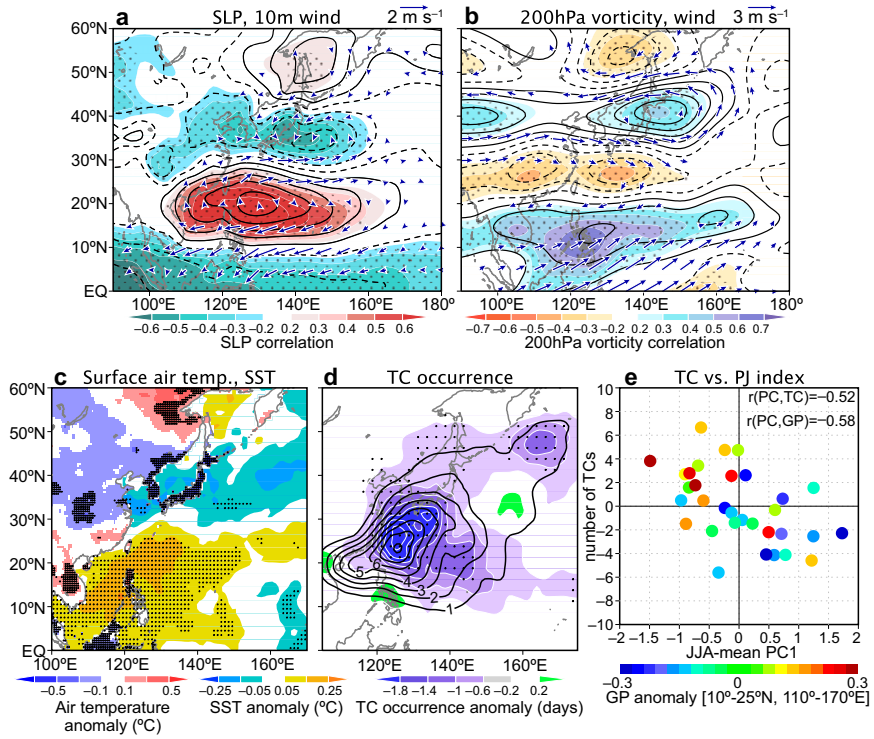


**Fig. S1.** Observed anomalies associated with the PJ pattern. (*A*) SLP (shading, correlations; contours, regressed anomalies for ±0.1, ±0.3, ±0.5, … hPa). The NWP (0°–60°N, 100°–160°E) average has been subtracted before being correlated/regressed. (*B*) Vorticity (200 hPa) (shading, correlations; contours, regressed anomalies for ±0.5, ±1.5, ±2.5, … $\times 10^{-6}$ $s^{-1}$). Arrows show regressed wind velocity anomalies at (*A*) 10 m and (*B*) 200 hPa. (*C*) Regressed anomalies of land-surface air temperature and SST. (*D*) Regressed anomalies (shading) and climatology (contour) of TC occurrence. *A*–*D* are plotted with respect to PC1. (*E*) Scatter diagram between PC1 and number of TCs, with colors indicating GP anomalies over [10°–25°N, 110°–170°E]. *A*–*C* are monthly values and *D* and *E* are based on JJA mean. Stippling indicates 95% confidence of shaded fields.

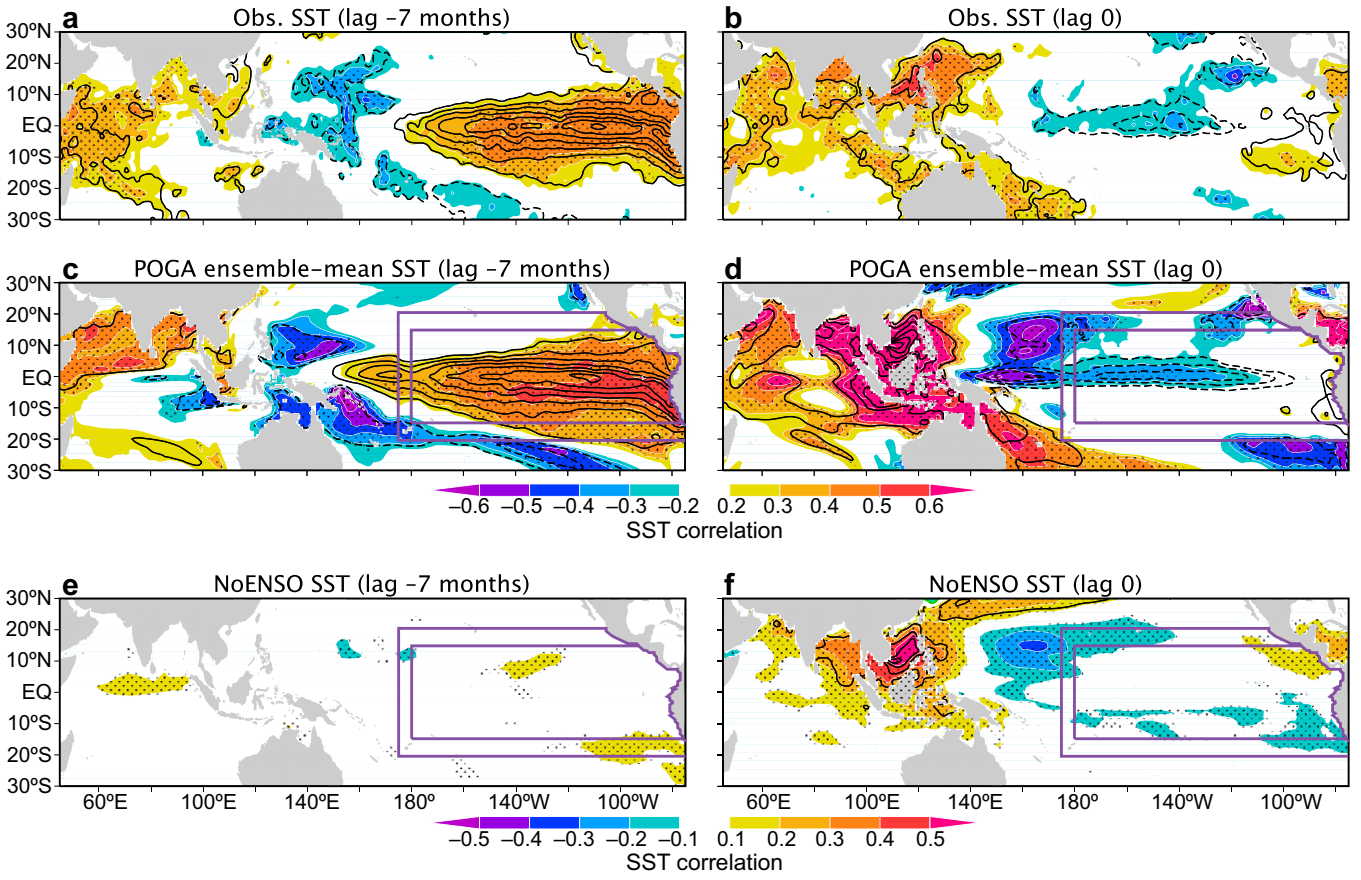


**Fig. S2.** (*A*–*F*) Lagged correlations (shading) and regressed anomalies (contours for ±0.1, ±0.2, ±0.3, . . . °C) of SST with respect to the PJ PC1s based on (*A* and *B*) observations, (*C* and *D*) POGA ensemble mean, and (*E* and *F*) NoENSO. (*A*, *C*, and *E*) Lag −7 mo; (*B*, *D*, and *F*) lag 0. Stippling indicate 95% statistical confidence. Boxes with purple lines in *C*–*F* show the SST-restoring region in POGA and NoENSO experiments. Color scales are different between *A*–*D* and *E* and *F*.

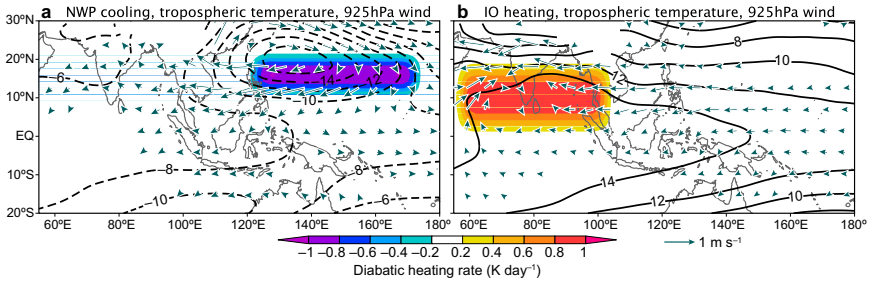


**Fig. S3.** (*A* and *B*) Dynamical responses to (*A*) diabatic cooling over the tropical NWP and (*B*) diabatic heating over the northern IO, based on LBM experiments. Shown are distributions of diabatic heating at the $\sigma = 0.45$ level (shading) and responses in tropospheric temperature (contours, in meters) and 925-hPa wind velocity (arrows). Here tropospheric temperature is derived from thickness between 250 and 850 hPa geopotential height.

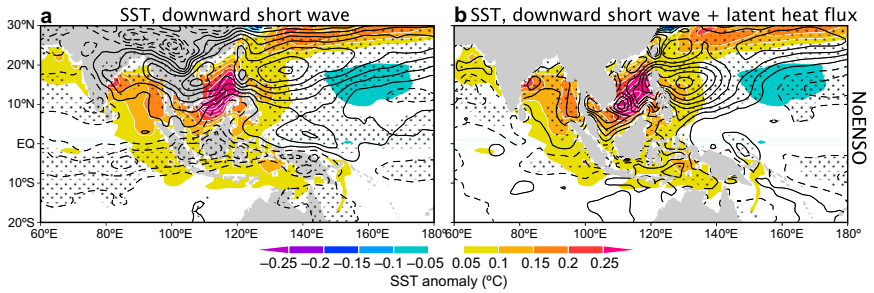


**Fig. S4.** (*A* and *B*) As in Fig. 4*A*, but contours show (*A*) downward shortwave radiation anomalies at the surface and (*B*) their sum with latent heat flux anomalies shown in Fig. 4*A*.

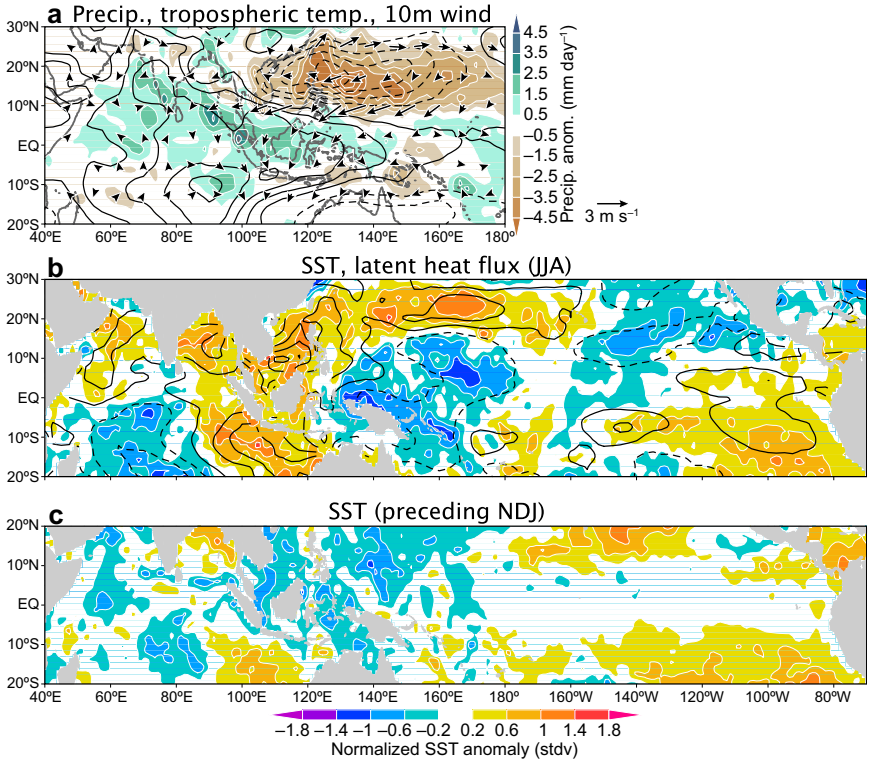


**Fig. S5.** Composited observational anomalies in JJA for eight PJ events in non-ENSO and weak ENSO summers. (*A*) Precipitation (shading), tropospheric temperature (contours), and 10-m wind (arrows); (*B*) SST (shading) and latent heat flux (contour) in simultaneous JJA; (*C*) SST in preceding NDJ. Tropospheric temperature and SST anomalies are normalized before being composited. Contours are drawn for (*A*) ±0.3, ±0.6, ±1.2, … and (*B*) ±5, ±15, ±25, … $W \cdot m^{-2}$.

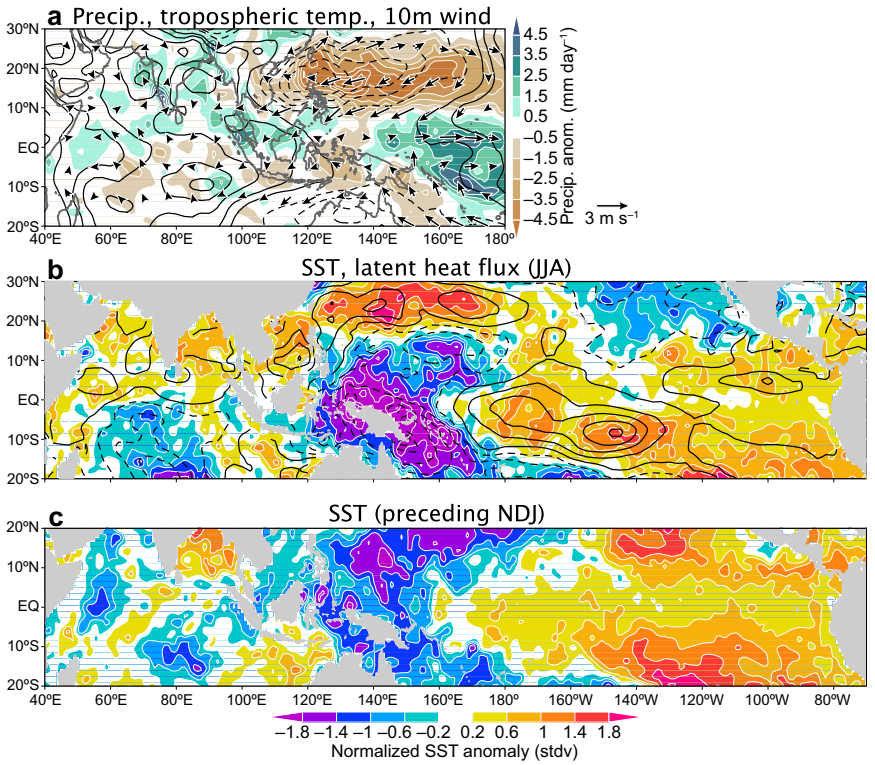


**Fig. S6.** (*A–C*) Same as Fig. S5 *A–C*, respectively, but composited for five PJ events with a severer criteria for non-ENSO years.

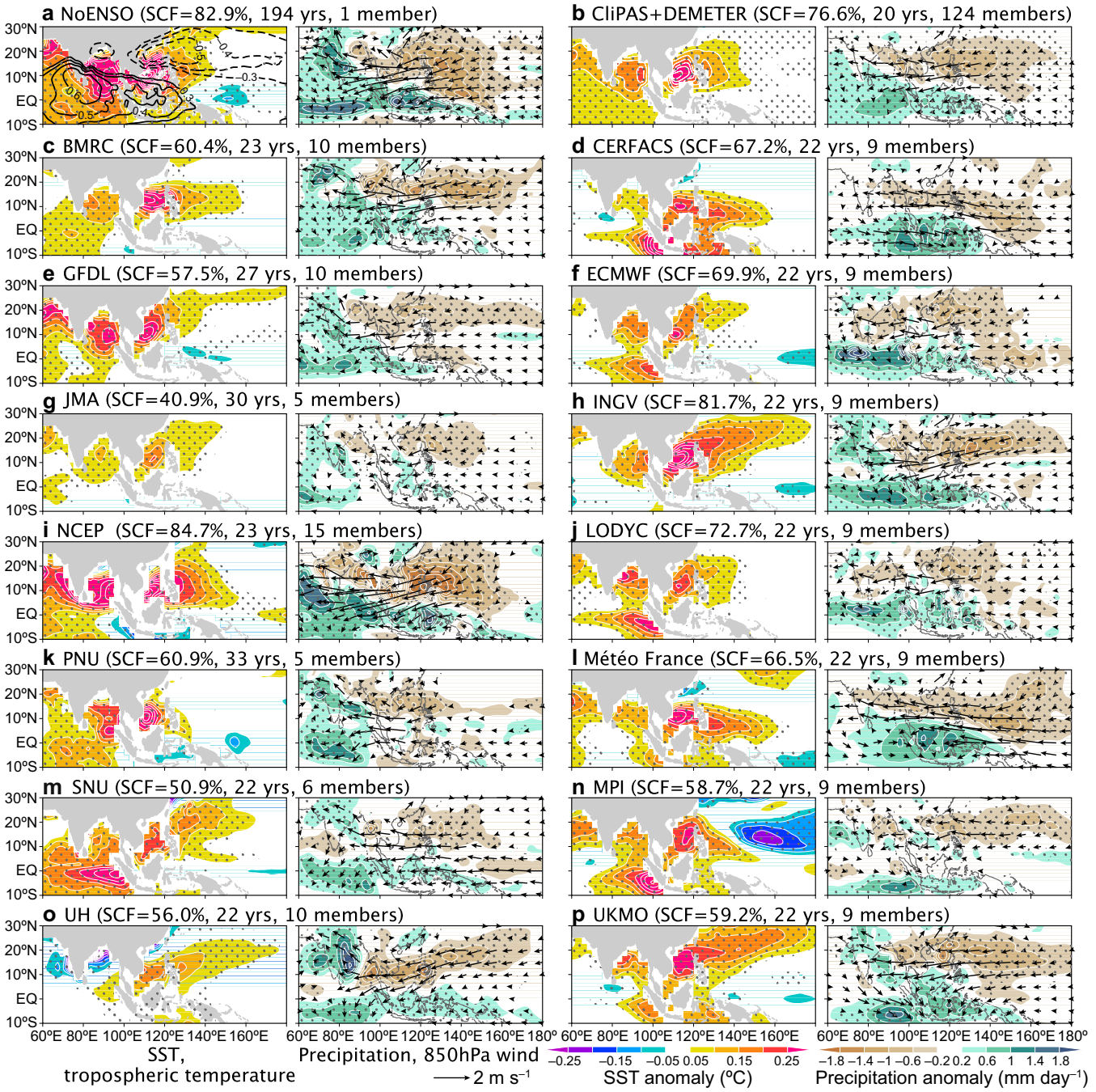


**Fig. S7.** (*A*–*P*) PJIO-coupled mode extracted as SVD1s of IO SST and NWP 850-hPa vorticity in JJA in (*A*) NoENSO and intermember variance of (*B*) the CliPAS and DEMETER grand ensemble and (*C*–*P*) individual prediction models. Shown are regressed anomalies of (*Left*) SST and (*Right*) precipitation (shading) and 850-hPa wind velocity (arrows). Stippling indicates 95% statistical confidence of shaded fields. Contours in *A*, *Left* indicate correlations of tropospheric temperature evaluated after its tropical (30°S–30°N) average has been subtracted. Squared covariance fraction (SCF) is also indicated.

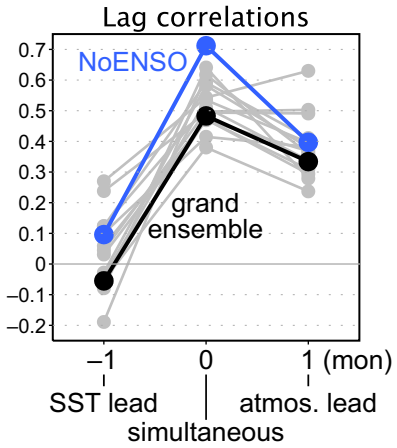


**Fig. S8.** Lead–lag correlations of vorticity and SST time series of SVD1s in NoENSO (blue), CliPAS and DEMETER grand ensemble of intermember variability (black), and intermember variability of individual prediction models (gray).

**Table S1. Spatial correlation coefficients of the model and observed EOF1 patterns with respect to the EOF1 pattern of POGA total variability**

| EOF1 pattern | Correlation coefficients |
|---|---|
| Observations | 0.88 |
| POGA | |
| Ensemble mean | 0.89 |
| Intermember | 0.92 |
| NoENSO | 0.91 |
| aCLIM | 0.74 |